

# Polarization control of RABBITT in noble gas atoms

Anatoli S. Kheifets<sup>†</sup> and Zhongtao Xu

Fundamental and Theoretical Physics, Research School of Physics,  
The Australian National University, Canberra 2601, Australia

E-mail: <sup>†</sup>a.kheifets@anu.edu.au

## Abstract.

The mutual angle formed by the non-collinear polarization axes of two laser pulses is used to control two-photon XUV+IR ionization of noble gas atoms in the process of reconstruction of attosecond bursts by beating of two-photon transitions (RABBITT). The magnitude and the phase of this beating can be controlled very efficiently by the mutual polarization angle. The mechanism of this control can be understood within the lowest order perturbation theory and the soft photon approximation. We offer a very sensitive test on the polarization control of the angular dependent RABBITT process which validates our numerical simulations. We apply this test to the recent theoretical and experimental results of polarization controlled RABBITT on hydrogen and helium by Boll *et al.*, Phys. Rev. A 107, 043113 (2023) and heavier noble gases by Jiang *et al.*, Nature Comms. 13, 5072 (2022).

## 1. Introduction

Two-color two-photon extreme ultraviolet and infrared (XUV+IR) photoionization has been applied recently for studying ultrafast electron dynamics on the attosecond time scale. Reconstruction of attosecond bursts by beating of two-photon transitions (RABBITT) (Paul *et al* 2001, Mairesse *et al* 2003) is one practical realization of this technique. In RABBITT, two collinearly polarized XUV and IR laser pulses with a variable delay are used to ionize the target atom and to steer emitted photoelectrons. The two-photon ionization yield oscillates with twice the IR photon frequency as the XUV/IR pulse delay varies. The phase of this oscillation encodes the timing of the XUV ionization (Véniard *et al* 1996, Dahlström *et al* 2013). Both the phase and magnitude of the RABBITT oscillation depend sensitively on the photoelectron escape angle relative to the common polarization axis of the XUV and IR pulses (Heuser *et al* 2016, Ivanov & Kheifets 2017, Bray *et al* 2018).

An additional control of two-color photoionization can be gained by relaxing the IR polarization direction and allowing its rotation relative to the XUV polarization axis (O’Keeffe *et al* 2004, Meyer *et al* 2008, Meyer *et al* 2010, Leitner *et al* 2015, Boll *et al* 2020). Recently, such a polarization control was implemented in RABBITT. Jiang *et al* (2022) demonstrated the so-called “atomic partial wave meter” where non-collinear partial waves with magnetic projections  $M \neq 0$  increase their presence gradually as the mutual polarization axes angle grows. Boll *et al* (2023) demonstrated an appearance of an additional set of angular nodes of the RABBITT amplitude in  $s$ -electron targets (H and He).

In the present work, we expand these initial investigations of polarization controlled RABBITT. In our theoretical modeling we use a numerical solution of the time-dependent Schrödinger equation (TDSE) to generate the angular-dependent phase and magnitude of the RABBITT oscillations in helium, neon and argon. In addition, we employ the lowest order perturbation theory (LOPT) (Véniard *et al* 1996, Dahlström *et al* 2013) and the soft photon approximation (SPA) (Maquet & Taïeb 2007) to provide qualitative interpretation of our numerical results. While we confirm the angular node structure of the RABBITT amplitude in  $s$ -electron targets (H and He) as reported by Boll *et al* (2023), the additional nodes are missing in heavier noble gases (Ne and Ar). This is explained within the SPA in which the RABBITT amplitude possesses the angular symmetry of XUV ionization  $1 + \beta P_2(\cos\theta)$  modulated by the IR angular factor  $\cos^2(\theta - \Theta)$ . Here  $\theta$  is the photoelectron escape angle and  $\Theta$  is the IR polarization axis angle. Both angles are counted relative to the XUV polarization direction which is taken as the quantization axis. In  $s$ -electron targets (H and He) the angular anisotropy parameter  $\beta = 2$  and the XUV angular factor reduces to  $\cos^2\theta$  which possesses an angular node. In  $p$  valence shells of heavier noble gases (Ne and Ar),  $\beta < 2$  and the XUV angular factor remains finite. Owing to the XUV+IR angular structure, the angular dependent RABBITT phase in H and He remains symmetric relative to the angle  $\theta - \Theta/2 = 90^\circ$  whereas it shows the angular symmetry relative to the angle  $\theta - \Theta = 90^\circ$  in Ne and Ar at small photoelectron energies where  $|\beta| \lesssim 1$ .

We confirm the gradual increase of partial waves with  $M \neq 0$  towards the orthogonal field configuration  $\Theta \rightarrow \pi/2$  when the IR angular factor reduces to  $\sin\theta \propto Y_{11}(\theta)$ . This increase is particularly graphical in  $s$ -electron targets. In all the targets, the photoelectron momentum distribution (PMD) displays a systematic angular rotation with the polarization control angle  $\Theta$ .

The rest of the paper is organized in the following way. In Sec. 2 we give a brief outline of our analytic tools (Sec. 2.1) and computational methods (Sec. 2.2). Sec. 3 contains our main numerical results presented consequently for helium, neon and argon. We conclude in Sec. 4 by outlining further extensions of the present study.

## 2. Theory

### 2.1. Analytic formulation

In a typical RABBITT measurement, an ionizing XUV attosecond pulse train (APT) is superimposed on an attenuated and variably delayed replica of the driving IR pulse. The XUV photon  $\Omega = (2q \pm 1)\omega$  is absorbed from the initial bound state and then is augmented by an IR photon absorption  $+\omega$  or emission  $-\omega$  leading to formation of the even order sideband (SB) in the photoelectron spectrum. The center of the IR pulse is shifted relative to the APT by a variable delay  $\tau$  such that the magnitude of a SB peak oscillates as

$$S_{2q}(\tau) = A + B \cos[2\omega\tau - C] . \quad (1)$$

The RABBITT parameters  $A$ ,  $B$  and  $C$  entering Eq. (1) can be expressed as

$$\begin{aligned} A &= \sum_{m_i} |\mathcal{M}_{m_i}^{(-)}(\mathbf{k})|^2 + |\mathcal{M}_{m_i}^{(+)*}(\mathbf{k})|^2 , \quad B = 2\text{Re} \sum_{m_i} [\mathcal{M}_{m_i}^{(-)}(\mathbf{k})\mathcal{M}_{m_i}^{(+)*}(\mathbf{k})] \\ C &= \arg \sum_{m_i} [\mathcal{M}_{m_i}^{(-)}(\mathbf{k})\mathcal{M}_{m_i}^{*(+)}(\mathbf{k})] \equiv 2\omega\tau_a . \end{aligned} \quad (2)$$



Here  $\mathcal{M}_{m_i}^{(\pm)}(\mathbf{k})$  are complex and angle-dependent amplitudes of two-photon ionization produced by adding (+) or subtracting (−) an IR photon, respectively. An incoherent summation over the angular momentum projection of the initial state  $m_i$  is explicit in Eq. (2). The atomic time delay  $\tau_a$  quantifies the timing of the XUV ionization process.

By adopting the soft photon approximation (SPA) (Maquet & Taïeb 2007) we can write

$$A, B \propto |J_1(\boldsymbol{\alpha}_0 \cdot \mathbf{k})|^2 |\langle f|z|i\rangle|^2 \propto [1 + \beta P_2(\cos \theta)] (\hat{\boldsymbol{\alpha}} \cdot \hat{\mathbf{k}})^2. \quad (3)$$

Here we make a linear approximation to the Bessel function as the parameter  $\alpha_0 = F_0/\omega^2 \ll 1$  in a weak IR field with a small magnitude  $F_0$ . The angular anisotropy  $\beta$  parameter defines the photoelectron angular distribution in single-photon XUV ionization. Derivation of Eq. (3) can be found in the Appendix of Bray *et al* (2018). Similar equations are used e.g. by Boll & Fojón (2017).

The angular dependence of the amplitudes  $\mathcal{M}_{\mathbf{k}}^{\pm}$  can be deduced from the LOPT expression (Dahlström *et al* 2013):

$$\begin{aligned} \mathcal{M}_{m_i}^{\pm}(\mathbf{k}) \propto \sum_{\lambda=l_i \pm 1} \sum_{L=\lambda \pm 1} \sum_{|M| \leq L; |\mu| \leq \lambda} (-i)^L e^{inL} Y_{LM}(\hat{k}) \int d^3\kappa \frac{\langle R_{kL}|r|R_{\kappa\lambda}\rangle \langle R_{\kappa\lambda}|r|R_{l_i m_i}\rangle}{E_i + \Omega^{\pm} - \kappa^2/2 - i\gamma} \\ \times \langle Y_{LM}|\hat{\boldsymbol{\alpha}} \cdot \hat{\mathbf{k}}|Y_{\lambda\mu}\rangle \langle Y_{\lambda\mu}|\cos\theta|Y_{l_i m_i}\rangle \end{aligned} \quad (4)$$

In the above expression,  $\langle n_i l_i|$ ,  $\langle \kappa\lambda|$  and  $\langle kL|$  are the initial, intermediate and final electron states defined by their linear and angular momenta, the latter are bound by the triangular angular momentum coupling rule. The XUV photon energy is  $\Omega^{\pm} = (2q \pm 1)\omega$  and  $i\gamma$  denotes the pole bypass in the complex energy plane. In the collinear case,  $M = 0$  and only the axially symmetry spherical harmonics  $Y_{L0}$  make their contribution.

To evaluate the angular integrals in Eq. (4) we transform the trigonometric functions into the matching spherical harmonics †. The product integral of three spherical harmonics is known analytically (Varshalovich *et al* 1988). In the simplest case of an  $s$ -electron target,  $m_i = 0$ ,  $\lambda = 1$  and  $L = \{0, 2\}$  which takes us to Eq. (3) of Jiang *et al* (2022)§:

$$\mathcal{M}_{\mathbf{k}}^{\pm} \propto \cos \Theta \left[ \frac{1}{\sqrt{3}} Y_{00}(\hat{k}) T_0^{\pm} + \frac{2}{\sqrt{15}} Y_{20}(\hat{k}) T_2^{\pm} \right] + \sin \Theta \frac{1}{\sqrt{10}} [Y_{21}(\hat{k}) - Y_{2-1}(\hat{k})] T_2^{\pm} \quad (5)$$

Here we reintroduced the radial factors  $T_L^{\pm}$  following notations of Boll *et al* (2023). The angular nodes of  $\mathcal{M}_{\mathbf{k}}^{\pm}$  correspond to the photoelectron emission angles  $\theta^{\pm}$  which satisfy Eqs. (11) and (12) of Boll *et al* (2023):

$$\cos(2\theta^{\pm} - \Theta) = - \left[ \frac{1}{3} + \frac{2 T_0^{\pm}}{3 T_2^{\pm}} \right] \cos \Theta, \quad \cos 2\theta^{\pm} = - \left[ \frac{1}{3} + \frac{2 T_0^{\pm}}{3 T_2^{\pm}} \right] \quad \text{for } \Theta = 0 \quad (6)$$

In the collinear case  $\Theta = 0$ , these nodes are controlled by the ratio  $T_0^{\pm}/T_2^{\pm}$ . In the non-collinear case, additional nodes appear which depend on the polarization control angle  $\Theta$ .

For a  $p$ -electron target, an angular node in  $\mathcal{M}_{m_i}^{\pm}(\mathbf{k})$  at a given  $m_i$  does not match nodes at other  $m_i$  values. For instance, in the simplest collinear  $\Theta = 0$  case, the node

† The corresponding evaluations are documented in the Mathematica notebook that can be found in the Supplementary Material.

§ The original equation of Jiang *et al* (2022) differs by an extra magnitude factor of  $1/\sqrt{3}$  and an alternative selection of the polar angle  $\phi \rightarrow \phi + \pi/2$

equations read

$$\cos(2\theta^\pm) = \begin{cases} \frac{1}{5} \left[ 1 - \frac{8}{3} \frac{T_1^\pm}{T_3^\pm} \right] \rightarrow -\frac{1}{3} & \text{as } T_1^\pm \rightarrow T_3^\pm \text{ for } m_i = 0 \\ -\frac{3}{5} \left[ 1 + \frac{2}{3} \frac{T_1^\pm}{T_3^\pm} \right] \rightarrow -1 & \text{as } T_1^\pm \rightarrow T_3^\pm \text{ for } m_i = 1 \end{cases} \quad (7)$$

In the  $m_i = 0$  case, the nodes approach asymptotically the magic angle of  $54.7^\circ$  whereas for  $m_i = 1$  these nodes tend asymptotically to  $90^\circ$ . Because of this mismatch, the magnitude  $B, C$  parameters remain nodeless.

## 2.2. Numerical methods

We follow closely the previous works by Bray *et al* (2018) and Kheifets & Bray (2021). In brief, we solve numerically the time-dependent Schrödinger equation (TDSE) in a single-active electron approximation: †

$$i\partial\Psi(\mathbf{r})/\partial t = \left[ \hat{H}_{\text{atom}} + \hat{H}_{\text{int}}(t) \right] \Psi(\mathbf{r}) . \quad (8)$$

Here the radial part of the atomic Hamiltonian

$$\hat{H}_{\text{atom}}(r) = -\frac{1}{2} \frac{d^2}{dr^2} + \frac{l(l+1)}{2r^2} + V(r) \quad (9)$$

contains an effective one-electron potential  $V(r)$  obtained by localization of the non-local Hartree-Fock potential (Wendin & Starace 1978). The Hamiltonian  $\hat{H}_{\text{int}}(t)$  describes interaction with the external field and is written in the velocity gauge

$$\hat{H}_{\text{int}}(t) = \mathbf{A}(t) \cdot \hat{\mathbf{p}} \quad , \quad \mathbf{A}(t) = - \int_0^t \mathbf{E}(t') dt' . \quad (10)$$

This external field is comprised of combination of XUV and IR fields. The XUV field is represented by an APT modeled by the vector potential

$$A_x(t) = \sum_{n=-5}^5 (-1)^n A_n \exp \left( -2 \ln 2 \frac{(t - nT/2)^2}{\tau_x^2} \right) \times \cos \left[ \omega_x (t - nT/2) \right] \quad (11)$$

with the magnitude of an  $n$ th pulselet

$$A_n = A_0 \exp \left( -2 \ln 2 \frac{(nT/2)^2}{\tau_T^2} \right) .$$

Here  $A_0$  is the vector potential peak value and  $T = 2\pi/\omega$  is the period of the IR field. The vector potential of the IR pulse is defined as

$$A(t) = A_0 \cos^2 \left( \frac{\pi(t - \tau)}{2\tau_{\text{IR}}} \right) \cos[\omega(t - \tau)] . \quad (12)$$

We select the fundamental IR frequency  $\omega = 1.55$  eV corresponding to the wavelength  $\lambda = 800$  nm. The XUV central frequency is set to  $\omega_x = 15\omega$  and the APT parameters are chosen as  $\tau_T = 5$  fs and  $\tau_x = 30$  as. The IR pulse length is defined by  $\tau_{\text{IR}} = 15$  fs. The intensity of the IR and XUV pulses is chosen in the range of  $1 \times 10^{10}$  W/cm<sup>2</sup>. Such an intensity is sufficiently low to stay within the LOPT boundaries.

The TDSE (8) is solved numerically by the spherical-coordinate implicit derivatives (SCID) computer code (Patchkovskii & Muller 2016). The PMD is obtained using the

† Here and throughout, we use the atomic units (a.u.) by setting  $e = m = \hbar = 1$ .

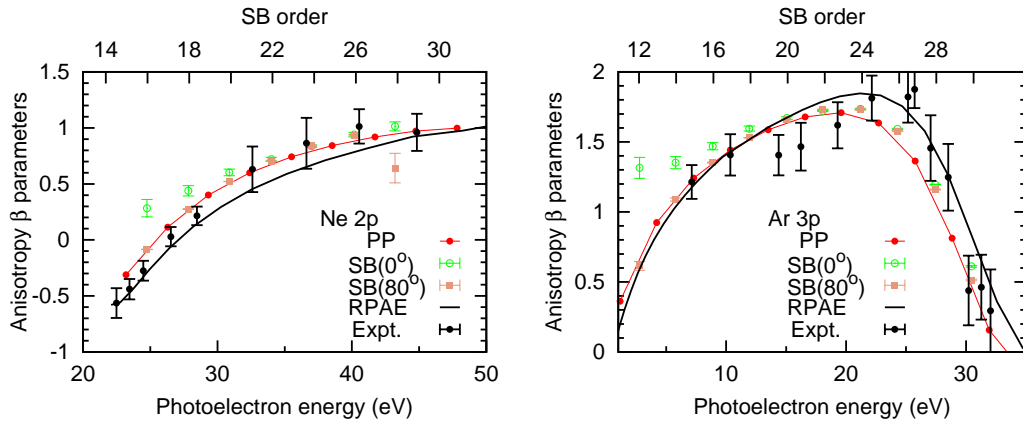


**Figure 1.** Angular anisotropy  $\beta$  parameter in Ne (left) and Ar (right) as extracted from the angular fitting to the primary harmonic peaks (PP), sidebands (SB) and the RPAE calculation. The SB data correspond to the polarization control angle of  $\Theta = 0$  and  $\Theta = 80^\circ$ . The experimental data are from Codling *et al* (1976) for Ne and Houlgate *et al* (1974) for Ar.

time-dependent surface flux (t-SURF) method (Tao & Scrinzi 2012, Morales *et al* 2016). The PMD can be expressed as the projection of the time-dependent wave function after the end of propagation on the basis of scattering states

$$P_{nl}(\mathbf{k}) = \sum_m \left| \langle \varphi_{\mathbf{k}}(r) | \Psi_{nlm}(\mathbf{r}, t \rightarrow \infty) \rangle \right|^2. \quad (13)$$

Here the indexes  $n, l, m$  denote the initial atomic bound state. The photoelectron momentum  $\mathbf{k}$  is defined in the Cartesian frame in which the  $\hat{z}$  axis is aligned with the polarization vector of the XUV pulses and the  $(x, z)$  plane contains both the polarization vectors of the XUV and IR pulses. Projection of the PMD on this plane serves to determine the angular profile of a given spectral feature:

$$S_N(\theta) = P_{nl}(k_x, k_y = 0, k_z) \quad , \quad \theta = \tan^{-1}(k_z/k_x) \quad , \quad (k_x^2 + k_z^2)/2 = N\omega - I_p. \quad (14)$$

Here  $N = 2q$  for a sideband and  $N = 2q \pm 1$  for a primary harmonic peak. In Eq. (14) the bound state indices  $nl$  are assumed on  $S_N(\theta)$  but dropped for brevity and  $I_p$  is the ionization potential of the target orbital. The  $k$ -grid is sufficiently dense to specify the angle  $\theta$  with a  $2^\circ$  increment.

The IR pulse is systematically shifted relative to the APT by a variable delay  $\tau$  in six increments by 10 a.u. This induces a time oscillation of the magnitude of each sideband  $S_{2q}$  which is fitted with Eq. (1) to obtain the angular dependent magnitude ( $A, B$ ) and phase ( $C$ ) parameters. The magnitude parameter  $B$  is then fitted with Eq. (3) to deduce the angular anisotropy  $\beta$  parameter. The same parameter can also be extracted from the angular variation of the prime harmonic peaks

$$S_{2q\pm 1}(\theta) \propto 1 + \beta P_2(\cos \theta) \quad (15)$$

In addition, the  $\beta$  parameter is calculated in the time-independent random phase approximation with exchange (RPAE) (Amusia 1990). Thus obtained  $\beta$  parameters in Ne and Ar are displayed in the left and right panels of Figure 1, respectively. The SB( $0^\circ$ ) and SB( $80^\circ$ )  $\beta$  parameters correspond to  $\Theta = 0$  and  $80^\circ$ . The latter set is in better agreement with other  $\beta$  values for both target atoms. This indicates that the validity of the SPA improves as the polarization control angle grows. The same conclusion was reached by Boll *et al* (2023).

### 3. TDSE results

#### 3.1. Helium

The PMD of He projected on the joint polarization plane is exhibited in the top row of panels in Figure 2. Each panel corresponds to a fixed polarization control angle  $\Theta$ . The sidebands are highlighted in the figure by applying a band pass filter

$$\bar{P}(k_x, k_z) = \sum_{2q} \int k^2 dk P(k_x, k_y = 0, k_z), \quad E_{2q} - \Gamma/2 < k_x^2 + k_z^2 < E_{2q} + \Gamma/2, \quad (16)$$

The filtered PMD (16) is zero outside the spectral width of the sideband  $\Gamma$ . Such a filtering masks the normally dominant prime harmonic peaks which are not sensitive to the polarization control. In the case of an *s*-electron targets (H and He),  $\beta = 2$  and the angular factor of Eq. (3) is reduced to  $\propto \cos^2 \theta \cos^2(\theta - \Theta)$ . This factor is visualized on the bottom row of panels in Figure 2. The sidebands at  $\Theta = 0$  have the  $\cos^4 \theta \propto |Y_{20}|^2$  angular pattern while at  $\Theta \rightarrow 90^\circ$  the sidebands acquire the  $\cos^2 \theta \sin^2 \theta \propto |Y_{21}|^2$  symmetry. This is in line with the “atomic partial wave meter” effect demonstrated by Jiang *et al* (2022).

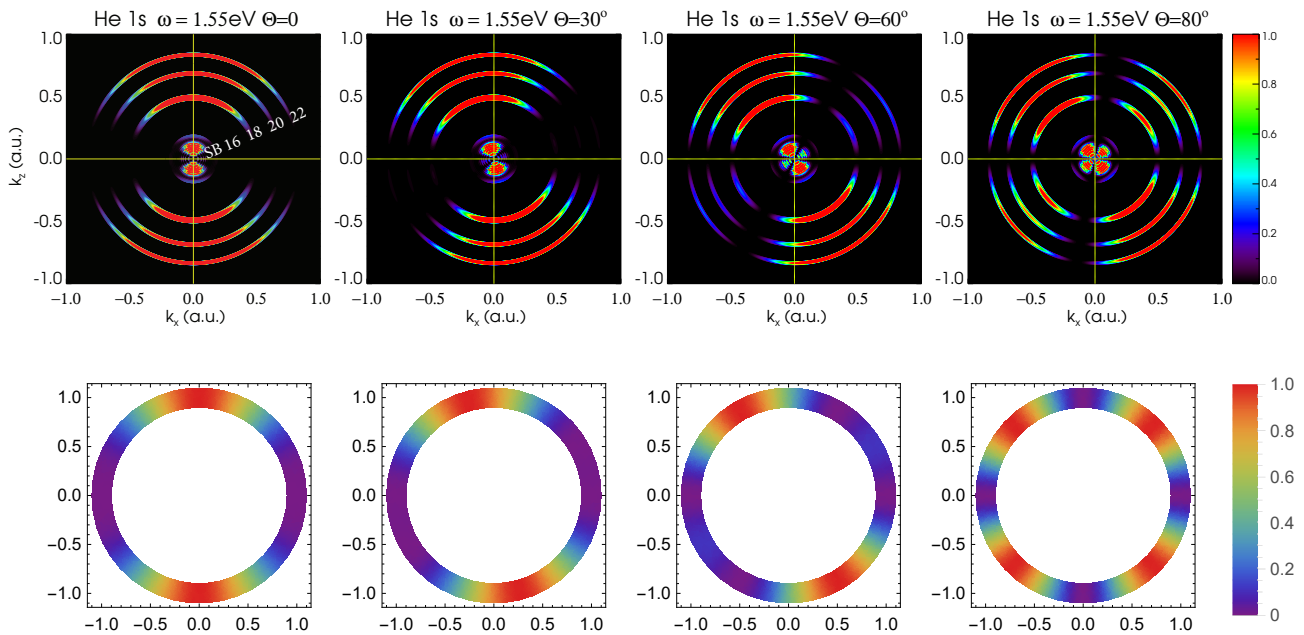


**Figure 2.** Top row: PMD of helium projected on the joint XUV/IR polarization plane at various angles  $\Theta$ . The XUV/IR time delay  $\tau = 0$  in all cases. The SB orders are as marked. Bottom row: graphical visualization of the angular factor  $\cos^2(\theta - \Theta) \cos^2 \theta$ .

We note that the primary harmonic peak PP15 submerges below the threshold in He. Correspondingly, the SB16 is formed by the under-threshold uRABBITT process. This process has been studied extensively in He (Swoboda *et al* 2010, Drescher *et al* 2022, Neorićić *et al* 2022, Autuori *et al* 2022) and heavier noble gases - Ne (Villeneuve *et al* 2017, Kheifets & Bray 2021, Kheifets 2021) and Ar (Kheifets 2023). While we do not observe a noticeable deviation of the angular symmetry of SB16 from other sidebands in He, this symmetry may differ in heavier noble gases.

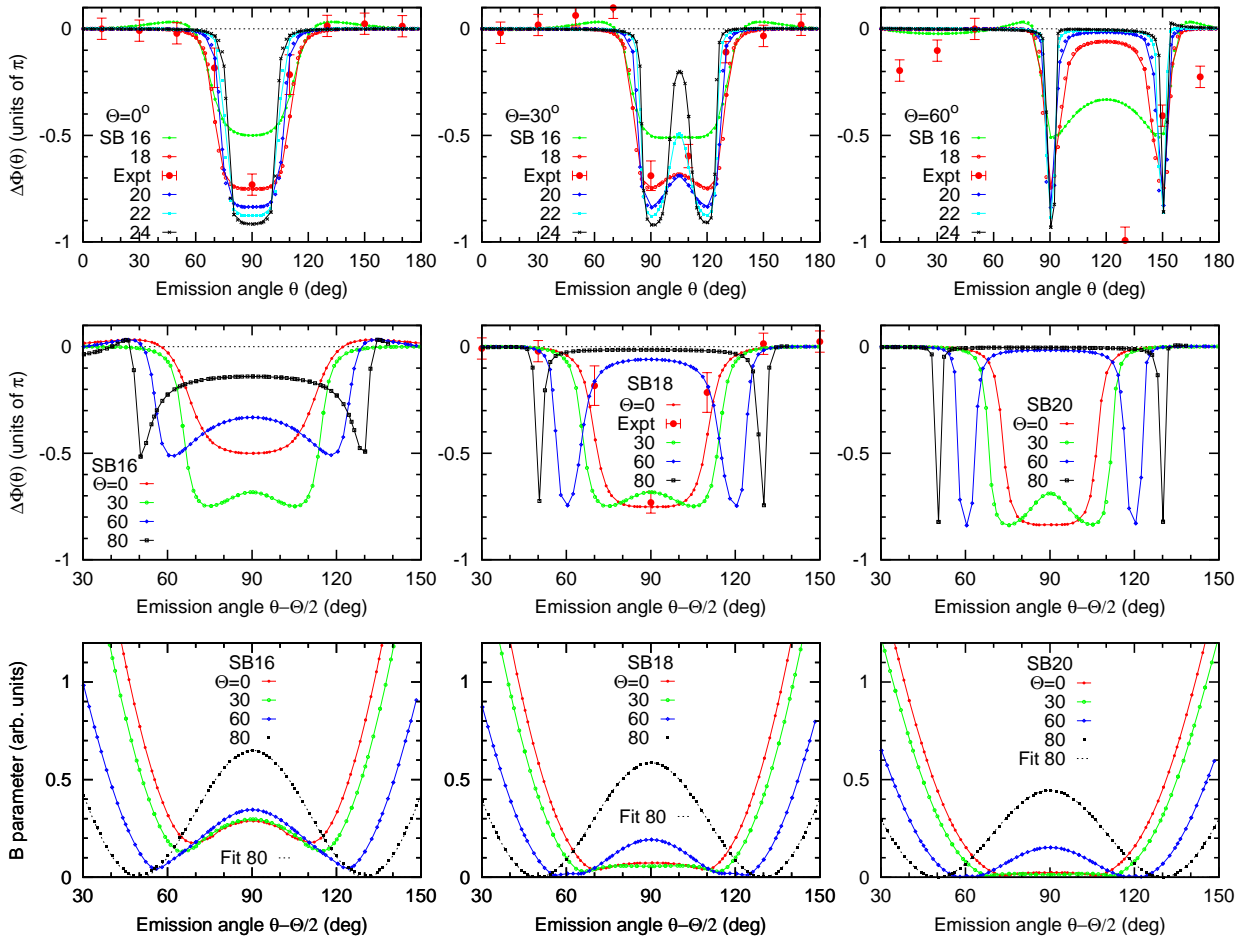


**Figure 3.** Angular dependence of RABBITT parameters in helium. Top row: RABBITT phase ( $C$ -parameter) counted relative to the zero emission angle  $\Delta\Phi(\theta) = \Phi(\theta) - \Phi(0)$  is shown for various SB orders at a fixed polarization control angle  $\Theta$ . The experimental data of Jiang *et al* (2022) for SB18 at the polarization control angles  $\Theta = 0, 20^\circ$  and  $54.7^\circ$  are shown with error bars. Middle row:  $\Delta\Phi$  is shown for several fixed SB orders while  $\Theta$  angle varies. The horizontal emission angle scale is shifted as  $\theta - \Theta/2$ . Bottom row:  $B$  parameter is shown for several fixed SB orders while  $\Theta$  angle varies. The dotted line shows the analytic fit with  $\cos^2\theta \cos^2(\theta - \Theta)$  for  $\Theta = 80^\circ$ .

Another set of the polarization control data is displayed in Figure 3 where we show the angular dependent RABBITT phase ( $C$ -parameter) and magnitude ( $B$ -parameter). The relative phase is counted relative to the XUV polarization direction  $\Delta\Phi(\theta) = \Phi(\theta) - \Phi(0)$ . In each panel of the top row, we display  $\Delta\Phi$  for a range of SB orders at a fixed  $\Theta$  value. Our results reproduce very closely the analogous set of data for hydrogen exhibited in Figs. 2 and 3 of Boll *et al* (2023). Although hydrogen is not a noble gas atom, the RABBITT process in H is very similar to that in He with a small adjustment of the photoelectron energy to account for different ionization potentials (Heuser *et al* 2016, Boll *et al* 2020, Boll *et al* 2023).

The characteristic feature of the angular dependent RABBITT phase is its jump by about one unit of  $\pi$  which is accompanied by a drop of the RABBITT magnitude. An angular node of the magnitude would have induced an exact  $\pi$  phase jump. In the collinear case  $\Theta = 0$ , the normally flat phase starts deviating from its polarization direction value near the “magic” angle of  $54.7^\circ$ . At this angle, the normally dominant  $d$ -wave passes through a kinematic node and the normally weak  $s$ -wave takes over. The phase jump becomes steeper as the SB order grows. This is explained by a gradual

convergence of the  $T_0$  and  $T_2$  factors in Eq. (6). The non-collinear case  $\Theta \neq 0$  is markedly different as the phase tends back to its  $\theta = 0$  value after the jump. This tendency is particularly clear at large angles  $\Theta$  when the second upwards phase jump occurs almost immediately after the first downwards jump. The latter behavior can be explained by the gradual increase of the  $M = \pm 1$  components in the final continuum which is not supported by the  $s$ -wave. Hence the  $d$ -wave remains dominant everywhere except for an immediate vicinity of its kinematic node. The experimental phases of Jiang *et al* (2022) for SB18 show a good agreement with our calculation in the collinear case  $\Theta = 0$ . However this agreement becomes poorer as the polarization control angle  $\Theta$  increases. The sparsity of the experimental data points does not allow to reveal the secondary phase jumps at large  $\Theta$  angles.

In the middle row of panels, we replot  $\Delta\Phi$  by adjusting the horizontal scale and shifting the photoelectron emission angle by  $\Theta/2$ . With this shift, all the angular distributions become perfectly centered with respect to the emission angle  $\theta - \Theta/2 = 90^\circ$ . Such a rigid alignment can be explained very simply by the RABBITT angular factor  $\cos(\theta - \Theta) \cos \theta \propto \cos(2\theta - \Theta) \propto \cos(\theta - \Theta/2)$ .

We note that the SB16 phase behavior as a function of the polarization control angle  $\Theta$  is noticeably different from that of higher order SB18 and SB20. The phase jump in SB16 is markedly smaller and the phase never returns to its  $\theta = 0$  value. This is another manifestation of the uRABBITT effect. We also note that the experimental data of Jiang *et al* (2022) for SB18 tend to cluster around the center at  $\theta - \Theta/2 = 90^\circ$  while the accompanying calculations of the same authors as well as that of Boll *et al* (2023) follow this pattern more clearly.

The bottom row of panels in Figure 3 displays the angular dependent  $B$  parameters on the adjusted angular scale. On this scale, the  $B$  parameters are perfectly centered relative to the angle  $\theta - \Theta/2 = 90^\circ$ . In the SB16 formed by the uRABBITT process, the  $B$  parameter falls sharply but does not reach zero at  $\Theta = 0$  and  $30^\circ$ . Accordingly, the phase displays a rather smooth angular variation by less than one unit of  $\pi$ . At larger angles  $\Theta = 60$  and  $80^\circ$ , an additional node appears and the phase displays a rather sharp oscillation. In the two conventional SB18 and SB20, the  $B$  parameters drop much closer to zero at  $\Theta = 0$  and  $30^\circ$  and the phase  $C$  parameter displays a steeper variation closer to one unit of  $\pi$ . The angular nodes are fully formed at  $\Theta = 60$  and  $80^\circ$  where they follow very closely the angular pattern  $\cos^2 \theta \cos^2(\theta - \Theta)$ . Accordingly, the phase oscillation becomes very sharp.



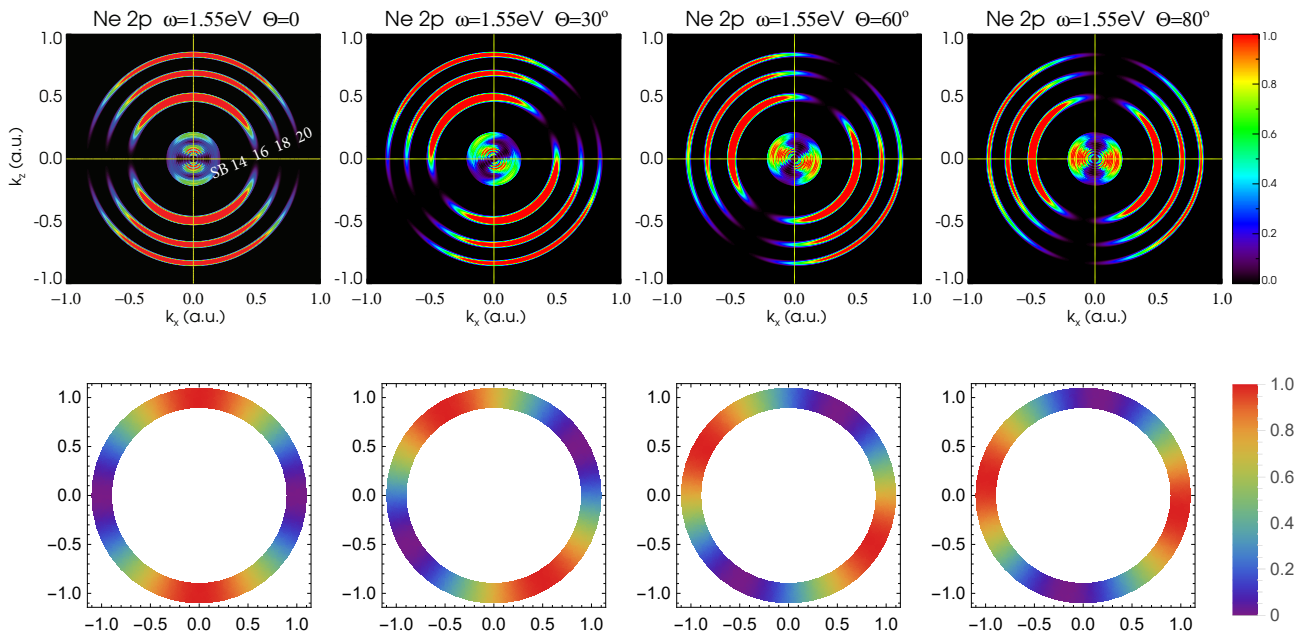


**Figure 4.** Top row: PMD of neon projected on the joint XUV/IR polarization plane at various angles  $\Theta$ . The XUV/IR time delay  $\tau = 0$  in all cases. The SB orders are as marked. Bottom row: graphical visualization of the angular factor  $\cos^2(\theta - \Theta)$ .

### 3.2. Neon

Polarization control of RABBITT in Ne is demonstrated in Figure 4. Here we display the filtered PMD (16) projected on the joint XUV/IR polarization plane at various angles  $\Theta$ . Similarly to Figure 2, the prime harmonic peaks are masked for clarity. These peaks show almost perfectly circular structure as the angular anisotropy is very small in Ne  $|\beta| \ll 1$  as is seen from the left panel of Figure 1. The SB's follow faithfully the  $\cos^2(\theta - \Theta)$  pattern as prescribed by the SPA.

The polarization control of the angular dependent RABBITT phase and magnitude parameters in Ne is demonstrated in Figure 5. As in Figure 3, the top row of panels shows  $\Delta\Phi(\theta)$  for a range of SB orders at various fixed  $\Theta$  values. In the middle row of panels, we group  $\Delta\Phi(\theta)$  for a given SB order while the polarization control angle  $\Theta$  varies. However, unlike in the middle panel of Figure 3, we shift the horizontal axis by the whole angle  $\Theta$  rather than by  $\Theta/2$ . Thus achieved phase centering near  $\theta - \Theta = 90^\circ$  is nearly perfect. Such an angular centering of the RABBITT phase in Ne can be understood within SPA. We note from the left panel of Figure 1 that  $|\beta| \ll 1$  for SB16 and SB18. Hence the angular dependence of the RABBITT spectrum is given by the IR factor  $\cos^2(\theta - \Theta)$  while the XUV angular factor remains flat.

We observe that SB14 displays a significantly broader angular variation which starts much further away from the center  $\theta - \Theta = 90^\circ$ . This is a manifestation of the uRABBITT process in Ne which is responsible for the formation of SB14 as the PP13 falls below the threshold. As in the case of He, the experimental data by Jiang *et al* (2022) for SB18 are close to our calculation in the collinear case but deviate significantly as the polarization control angle  $\Theta$  increases. We also note that the experimental data for Ne do not adhere to the  $\theta - \Theta = 90^\circ$  centering whereas the accompanying *R*-matrix calculation does display this centering.

The bottom row of panels in Figure 5 displays the angular dependent *B* parameters

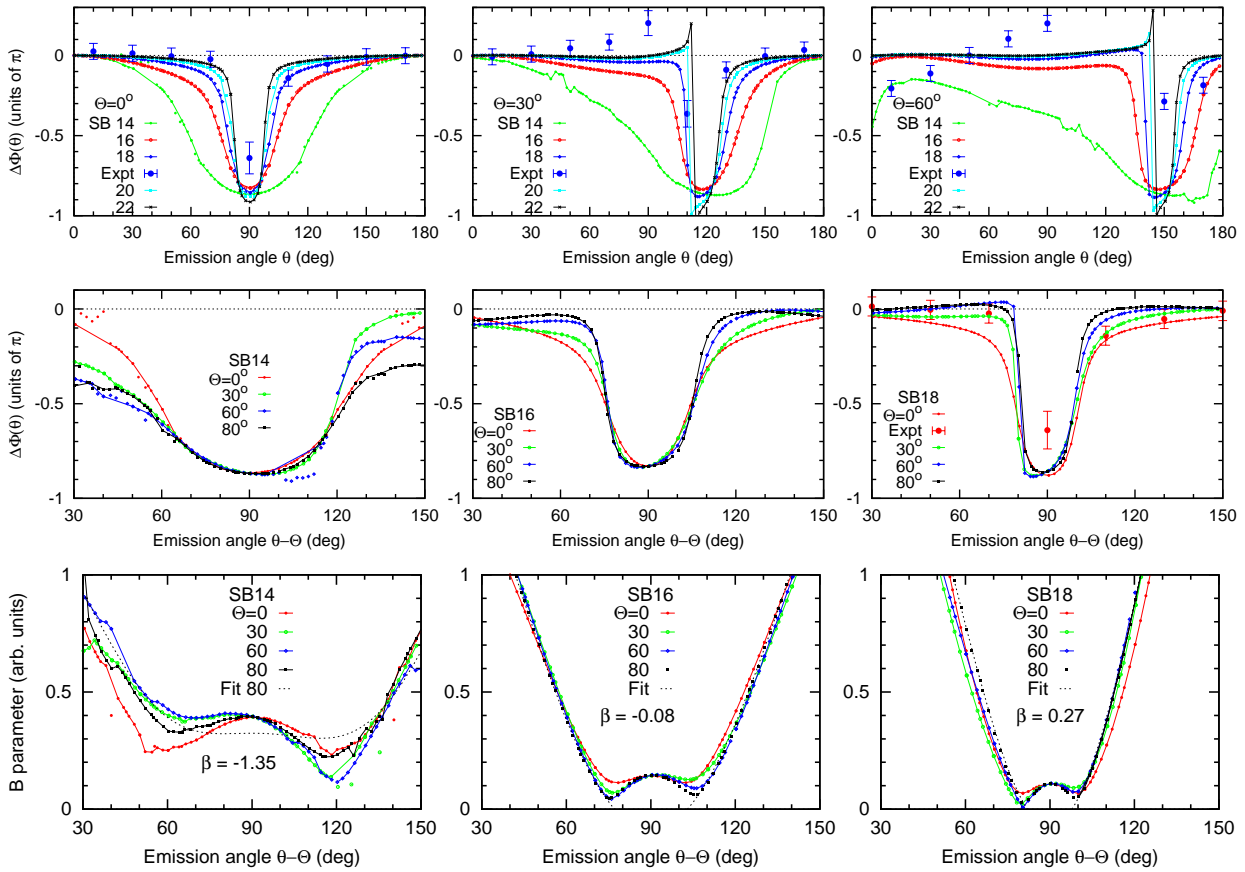


**Figure 5.** Same as Figure 3 for neon. Top row:  $\Delta\Phi$  is shown for various SB orders at a fixed polarization control angle  $\Theta$ . The experimental data of Jiang *et al* (2022) for SB18 at the polarization control angles  $\Theta = 0, 20^\circ$  and  $54.7^\circ$  are shown with error bars. Middle row:  $\Delta\Phi$  is shown for several fixed SB orders while  $\Theta$  angle varies. The horizontal emission angle scale is shifted as  $\theta - \Theta$ . Bottom row:  $B$  parameter is shown for several fixed SB orders while  $\Theta$  angle varies. The dotted line shows the analytic fit with  $[1 + \beta P_2(\cos\theta)] \cos^2(\theta - \Theta)$  for  $\Theta = 80^\circ$ . The corresponding  $\beta$  values are displayed.

on the adjusted angular scale. On this scale, the  $B$  parameters are centered relative to the angle  $\theta - \Theta = 90^\circ$ . This centering is more accurate in SB16 and 18 in comparison with the uRABBITT SB14. The latter is only centered in a close vicinity of  $90^\circ$ . In the SB16 formed by the uRABBITT process, the  $B$  parameter never falls close to zero. Accordingly, the phase varies rather smoothly on a wide angular range. In the conventional RABBITT SB16 and SB18, the magnitude  $B$  falls steeply towards the center  $\theta - \Theta = 90^\circ$  and almost reaches zero, especially for SB18. The  $\beta$  values extracted from the analytic fit with Eq. (3) at  $\Theta = 80^\circ$  are shown on each panel. For the uRABBITT SB14 this fit produces an unphysical result  $\beta < -1$ . This can be understood as the  $\beta$  parameterization is not applicable to a discrete-discrete XUV photon absorption responsible for the uRABBITT process. For conventional SB16 and 18, the  $\beta$  values are reasonable and close to those exhibited in the left panel of Figure 1. As  $\beta$  grows, the angular variation of the  $B$  and  $C$  parameters become sharper and centers closer to  $\theta - \Theta = 90^\circ$ .

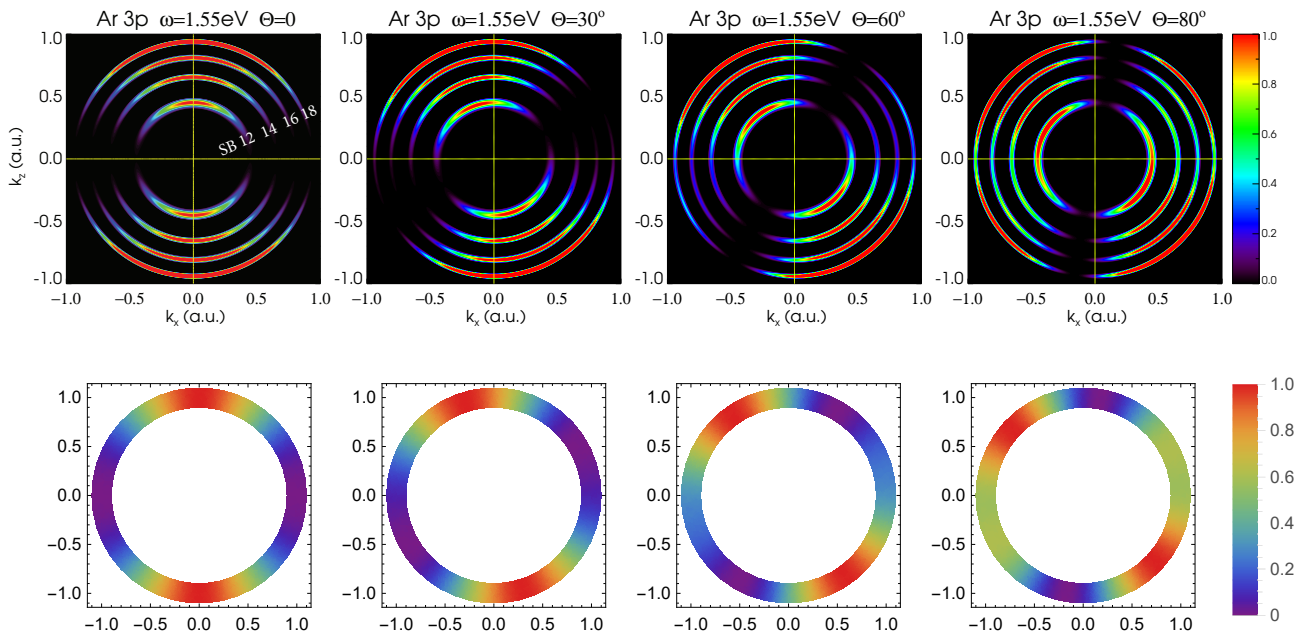


**Figure 6.** Top row: PMD of argon projected on the joint XUV/IR polarization plane at various angles  $\Theta$ . The XUV/IR time delay  $\tau = 0$  in all cases. The SB orders are as marked. Bottom row: graphical visualization of the angular factor  $[1 + \beta P_2(\cos \theta)] \cos^2(\theta - \Theta)$  with  $\beta = 1$ .

### 3.3. Argon

The polarization control of RABBITT in Ar is demonstrated in Figs. 6 and 7. In the case of Ar, all the considered sidebands are formed by a conventional RABBITT process. The under-threshold uRABBITT in Ar can be observed at 400 nm (Kheifets 2023) but does not manifest itself in the present case at 800 nm. As is seen from the right panel of Figure 1,  $\beta \simeq 1$  for the shown SB's in Ar. Accordingly, the PMD follows the  $[1 + P_2(\cos \theta)] \cos^2(\theta - \Theta)$  angular pattern which is displayed on the bottom panel of Figure 6.

The angular dependent RABBITT parameters in Ar are visualized in Figure 7. The top row of panels displays the phases of several SB's at a fixed polarization control angle  $\Theta$ . In the middle panel, the SB order is fixed while the angle  $\Theta$  varies. Similarly to Ne, the RABBITT phases are perfectly centered relative to the angle  $\theta - \Theta = 90^\circ$ . The width of the angular variation relative to this angle decreases systematically as the angle  $\Theta$  grows. The experimental data by Jiang *et al* (2022) agree well with our calculation in the collinear case but they become too sparse to reproduce a rather narrow angular variation near  $\theta - \Theta = 90^\circ$  for larger  $\Theta$ . In the meantime, the theoretical results accompanying the experiment by Jiang *et al* (2022) conform to the  $\theta - \Theta = 90^\circ$  centering.

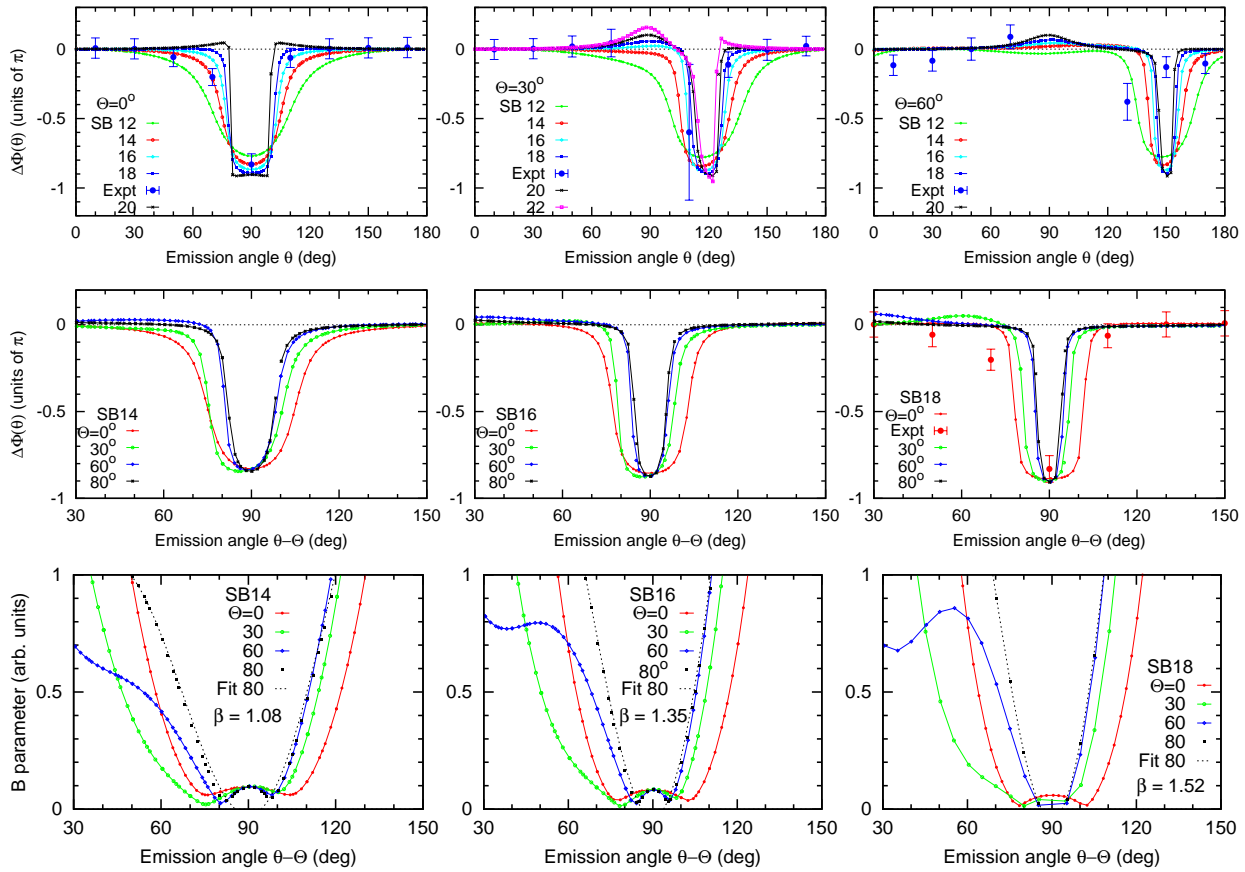


**Figure 7.** Same as Figure 5 for argon. Top row:  $\Delta\Phi$  is shown for various SB orders at a fixed polarization control angle  $\Theta$ . The experimental data of Jiang *et al* (2022) for SB18 at the polarization control angles  $\Theta = 0, 20^\circ$  and  $54.7^\circ$  are shown with error bars. Middle row:  $\Delta\Phi$  is shown for several fixed SB orders while  $\Theta$  angle varies. The horizontal emission angle scale is displaced as  $\theta - \Theta$ . Bottom row:  $B$  parameter is shown for several fixed SB orders while  $\Theta$  angle varies. The dotted line shows the analytic fit with  $[1 + \beta P_2(\cos\theta)] \cos^2(\theta - \Theta)$  for  $\Theta = 80^\circ$ . The corresponding  $\beta$  values are displayed.

The bottom row of panels of Figure 7 shows the angular variation of the magnitude  $B$  parameters which are fitted with Eq. (3) at  $\Theta = 80^\circ$ . The corresponding  $\beta$  parameters agree well with other theoretical and experimental values displayed in the right panel of Figure 1. As  $\beta$  increases, the angular dependence of the  $B$  and  $C$  parameters sharpens, especially at larger polarization control angles  $\Theta$ .

#### 4. Conclusion

In the present work we study systematically the polarization control of RABBITT in noble gas atoms, from He to Ar. As the control variable, we use the mutual angle  $\Theta$  formed by the non-collinear XUV/IR polarization axes. Our analysis is based on the numerical solution of the TDSE driven by a combination of XUV and IR pulses at a variable delay. We also invoke the LOPT and SPA to interpret our numerical results qualitatively.

We visualize the polarization control of RABBITT by two sets of graphical presentations. In the panoramic view, we display the PMD projected on the joint XUV/IR polarization plane and highlight the SB angular symmetry by masking the

normally stronger prime harmonic peaks. While the latter peaks are insensitive to the polarization control, the SB's can be easily manipulated. Their angular symmetry follows closely the predictions of SPA for all target atoms.

In a more detailed view, we analyze the angular dependent magnitude and phase of the RABBITT oscillations. This analysis is greatly simplified by an angular shift of the photoelectron emission angle  $\theta$  which centers the RABBITT parameters relative to the angle  $\theta - \Theta/2 = 90^\circ$  in H and He and that of  $\theta - \Theta = 90^\circ$  in Ne and Ar. Such a centering is explained by the corresponding values of the angular anisotropy  $\beta$  parameter. While  $\beta = 2$  in *s*-electron targets,  $\beta \ll 1$  in Ne and  $\beta \lesssim 1$  in Ar at small photoelectron energies that we analyze. The experimental data of Jiang *et al* (2022) are too sparse to subject them to a rigid centering test whereas the accompanying theory as well as the calculations by Boll *et al* (2023) do comply with this test. We hope that experimental data on a denser angular grid with better statistics will appear soon to conduct a more conclusive test. We also plan to extend our studies towards the diatomic molecules such as H<sub>2</sub> in which the PMD demonstrates much more complicated angular structure (Serov & Kheifets 2017, Serov & Kheifets 2023). We expect that the polarization control of RABBITT in H<sub>2</sub> would provide a deeper insight into this process.

### Acknowledgment

We gratefully acknowledge support of the National Computational Infrastructure facility (NCI Australia) which was instrumental for this work.

## Bibliography

- Amusia M Y 1990 *Atomic photoeffect* Plenum Press New York
- Autuori A, Platzer D, Lejman M, Gallician G, Maëder L, Covolo A, Bosse L, Dalui M, Bresteau D, Hergott J F, Tcherbakoff O, Marroux H J B, Lorient V, Lépine F, Poisson L, Taïeb R, Caillat J & Salières P 2022 Anisotropic dynamics of two-photon ionization: An attosecond movie of photoemission *Science Advances* **8**(12), eabl7594
- Boll D I R & Fojón O A 2017 Attosecond polarization control in atomic rabbit-like experiments assisted by a circularly polarized laser *J. Phys. B* **50**(23), 235604
- Boll D I R, Martini L, Fojón O A & Palacios A 2020 Off-resonance-enhanced polarization control in two-color atomic ionization *Phys. Rev. A* **101**, 013428
- Boll D I R, Martini L, Palacios A & Fojón O A 2023 Two-color polarization control of angularly resolved attosecond time delays *Phys. Rev. A* **107**, 043113
- Bray A W, Naseem F & Kheifets A S 2018 Simulation of angular-resolved RABBITT measurements in noble-gas atoms *Phys. Rev. A* **97**, 063404
- Codling K, Houlgate R G, West J B & Woodruff P R 1976 Angular distribution and photoionization measurements on the 2p and 2s electrons in neon *J. Phys. B* **9**(5), L83
- Dahlström *et al* J M 2013 Theory of attosecond delays in laser-assisted photoionization *Chem. Phys.* **414**, 53 – 64
- Drescher L, Witting T, Kornilov O & Vrakking M J J 2022 Phase dependence of resonant and antiresonant two-photon excitations *Phys. Rev. A* **105**, L011101
- Heuser S, Jiménez Galán A, Cirelli C, Marante C, Sabbar M, Boge R, Lucchini M, Gallmann L, Ivanov I, Kheifets A S, Dahlström J M, Lindroth E, Argenti L, Martín F & Keller U 2016 Angular dependence of photoemission time delay in helium *Phys. Rev. A* **94**, 063409
- Houlgate R G, Codling K, Marr G V & West J B 1974 Angular distribution and photoionization cross section measurements on the 3p and 3s subshells of argon *J. Phys. B* **7**(17), L470
- Ivanov I A & Kheifets A S 2017 Angle-dependent time delay in two-color XUV+IR photoemission of He and Ne *Phys. Rev. A* **96**, 013408
- Jiang W, Armstrong G S J, Tong J, Xu Y, Zuo Z, Qiang J, Lu P, Clarke D D A, Benda J, Fleischer A, Ni H, Ueda K, van der Hart H W, Brown A C, Gong X & Wu J 2022 Atomic partial wave meter by attosecond coincidence metrology *Nature Communications* **13**, 5072
- Kheifets A 2021 Revealing the target electronic structure with under-threshold RABBITT *Atoms* **9**(3), 66
- Kheifets A S 2023 Under-threshold rabbit in argon *J. Phys. B* **56**(9), 095201
- Kheifets A S & Bray A W 2021 RABBITT phase transition across the ionization threshold *Phys. Rev. A* **103**, L011101
- Leitner T, Taïeb R, Meyer M & Wernet P 2015 Probing photoelectron angular distributions in molecules with polarization-controlled two-color above-threshold ionization *Phys. Rev. A* **91**, 063411
- Mairesse Y, de Bohan A, Frasninski L J, Merdji H, Dinu L C, Monchicourt P, Breger P, Kovacev M, Taïeb R, Carré B, Muller H G, Agostini P & Salières P 2003 Attosecond synchronization of high-harmonic soft x-rays *Science* **302**(5650), 1540–1543
- Maquet A & Taïeb R 2007 Two-colour ir+xuv spectroscopies: the soft-photon approximation *J. Modern Optics* **54**(13-15), 1847–1857
- Meyer M, Costello J T, Düsterer S, Li W B & Radcliffe P 2010 Two-colour experiments in the gas phase *J. Phys. B* **43**(19), 194006
- Meyer M, Cubaynes D, Glijer D, Dardis J, Hayden P, Hough P, Richardson V, Kennedy E T, Costello J T, Radcliffe P, Düsterer S, Azima A, Li W B, Redlin H, Feldhaus J, Taïeb R, Maquet A, Grum-Grzhimailo A N, Gryzlova E V & Strakhova S I 2008 Polarization control in two-color above-threshold ionization of atomic helium *Phys. Rev. Lett.* **101**, 193002
- Morales F, Bredtmann T & Patchkovskii S 2016 iSURF: a family of infinite-time surface flux methods *J. Phys. B* **49**(24), 245001
- Neoričić L, Busto D, Laurell H, Weissenbilder R, Ammitzböll M, Luo S, Peschel J, Wikmark H, Lahl J, Maclot S, Squibb R J, Zhong S, Eng-Johnsson P, Arnold C L, Feifel R, Gisselbrecht M, Lindroth E & L’Huillier A 2022 Resonant two-photon ionization of helium atoms studied by attosecond interferometry *Frontiers in Physics*
- O’Keeffe P, López-Martens R, Mauritsson J, Johansson A, L’Huillier A, Véniard V, Taïeb R, Maquet A & Meyer M 2004 Polarization effects in two-photon nonresonant ionization of argon with



- extreme-ultraviolet and infrared femtosecond pulses *Phys. Rev. A* **69**, 051401
- Patchkovskii S & Muller H 2016 Simple, accurate, and efficient implementation of 1-electron atomic time-dependent Schrödinger equation in spherical coordinates *Computer Physics Communications* **199**, 153 – 169
- Paul P M, Toma E S, Breger P, Mullot G, Augé F, Balcou P, Muller H G & Agostini P 2001 Observation of a train of attosecond pulses from high harmonic generation *Science* **292**(5522), 1689–1692
- Serov V V & Kheifets A S 2017 Time delay in XUV/IR photoionization of H<sub>2</sub>O *J. Chem. Phys.* **147**(20), 204303
- Serov V V & Kheifets A S 2023 XUV ionization of the H<sub>2</sub> molecule studied with attosecond angular streaking *J. Phys. B* **56**(2), 025601
- Swoboda M, Fordell T, Klünder K, Dahlström J M, Miranda M, Buth C, Schafer K J, Mauritsson J, L’Huillier A & Gisselbrecht M 2010 Phase measurement of resonant two-photon ionization in helium *Phys. Rev. Lett.* **104**, 103003
- Tao L & Scrinzi A 2012 Photo-electron momentum spectra from minimal volumes: the time-dependent surface flux method *New J. Phys.* **14**, 013021
- Varshalovich D A, Moskalev A N & Khersonskii V K 1988 *Quantum theory of angular momentum* 1st edn World Scientific Pub. Philadelphia
- Véniard V, Taïeb R & Maquet A 1996 Phase dependence of  $(n + 1)$ -color ( $n > 1$ ) ir-uv photoionization of atoms with higher harmonics *Phys. Rev. A* **54**, 721–728
- Villeneuve D M, Hockett P, Vrakking M J J & Niikura H 2017 Coherent imaging of an attosecond electron wave packet *Science* **356**(6343), 1150–1153
- Wendin G & Starace A F 1978 Perturbation theory in a strong-interaction regime with application to 4d-subshell spectra of Ba and La *J. Phys. B* **11**(24), 4119